The SπRIT Time Projection Chamber

J. Barney,[1,2,a] J. Estee,[1,2] W.G. Lynch (連致標),[1,2,b] T. Isobe (磯部忠昭),[3,c] G. Jhang (장진희),[1]
M. Kurata-Nishimura (倉田-西村美月),[3] A.B. McIntosh,[4] T. Murakami (村上哲也),[5,d] R. Shane,[1] S.
Tangwancharoen,[1] M.B. Tsang (曾敏兒),[1,2,e] G. Cerizza,[1] M. Kaneko (金子雅紀),[5,3] J.W. Lee (이정우),[6] C.Y.
Tsang (曾浚源),[1,2] R. Wang (王仁生),[1] C. Anderson,[1] H. Baba (馬場秀忠),[3] Z. Chajecki,[7] M. Famiano,[7] R.
Hodges-Showalter,[1] B. Hong (홍병식),[6] T. Kobayashi (小林俊雄),[8] P. Lasko,[9] J. Łukasik,[9] N. Nakatsuka (中塚
徳継),[3] R. Olsen,[4] H. Otsu (大津秀暁),[3] P. Pawłowski,[9] K. Pelczar,[10] H. Sakurai (櫻井博儀),[3] C. Santamaria,[1]
H. Setiawan,[1] A. Taketani (竹谷篤),[3] J.R. Winkelbauer,[1] Z. Xiao (肖志剛),[11] S.J. Yennello,[4] J. Yurkon,[1] and Y.
Zhang (张嫣)[11]

[1] *National Superconducting Cyclotron Laboratory, East Lansing, MI 48824, USA*
[2] *Department of Physics and Astronomy, Michigan State University, East Lansing, MI 48824 USA*
[3] *RIKEN Nishina Center, Hirosawa 2-1, Wako, Saitama 351-0198, Japan*
[4] *Cyclotron Institute, Texas A&M University, College Station, TX 77843, USA*
[5] *Department of Physics, Kyoto University, Kita-shirakawa, Kyoto 606-8502, Japan*
[6] *Department of Physics, Korea University, Seoul 02841, Republic of Korea*
[7] *Department of Physics, Western Michigan University, Kalamazoo, Michigan 49008 USA*
[8] *Department of Physics, Tohoku University, Sendai 980-8578, Japan*
[9] *Institute of Nuclear Physics PAN, ul. Radzikowskiego 152, 31-342 Kraków, Poland*
[10] *Gran Sasso National Laboratory - INFN, Via G. Acitelli 22, 67100 Assergi, L'Aquila AQ Italy*
[11] *Department of Physics, Tsinghua University, Beijing 100084, PR China*

The SAMURAI Pion Reconstruction and Ion-Tracker Time Projection Chamber (SπRIT TPC) was designed to enable measurements of heavy ion collisions with the SAMURAI spectrometer at the RIKEN Radioactive Isotope Beam Factory and provide constraints on the Equation of State of neutron-rich nuclear matter. The SπRIT TPC has a 50.5 cm drift length and an 86.4 cm × 134.4 cm pad plane with 12,096 pads that are equipped with the Generic Electronics for TPCs. The SπRIT TPC allows excellent reconstruction of particles and provides isotopic resolution for pions and other light charged particles across a wide range of energy losses and momenta. Details of the SπRIT TPC are presented, along with discussion of the TPC performance based on cosmic ray and charged particles emitted in heavy ion collisions.

Placing constraints on the density dependence of the symmetry energy term of the nuclear Equation of State (EoS) is an important research objective for both nuclear physics and astrophysics[1]. The SAMURAI Pion-Reconstruction and Ion-Tracker (SπRIT) Time Projection Chamber (TPC) was designed and constructed to be used as the primary tracking detector in a series of experiments designed to constrain the symmetry energy at about twice normal nuclear matter density[2]. Copious production of charged particles is anticipated in central collisions of heavy ion beams with energy ranges of 200–500 AMeV. The TPC design allows determination of Particle IDentification (PID) of charged pions and light charged particles up to Li by measuring their momentum distributions and energy losses in the gas. Initial design of the TPC and its specific requirements can be found in Ref. 2. This paper details the final design and actual construction of the SπRIT TPC, and discusses how the design was influenced by the experimental requirements. The TPC has been successfully deployed in a series of experiments to use pions to study the density dependence of symmetry energy[3,4].

This paper is organized as follows: A brief overview of the

TPC and operating principle, is followed by further detailed description of individual components provided in Section 1. The performance of the SπRIT TPC is demonstrated using cosmic muons and selected data from the experimental campaign in Section 2 followed by the conclusions.

The design and operating principles of the SπRIT TPC are illustrated by Fig. 1. To avoid strong $\vec{E} \times \vec{B}$ drift velocity effects, the main electric and magnetic fields in a TPC are usually parallel or antiparallel, linking the geometry of a TPC design strongly to the geometry of its magnet. The SπRIT TPC is rectangular, designed to work with the Superconducting Analyzer for MUlti-particles from RAdioIsotope beams (SAMURAI) dipole magnet[5]. Its pad plane and wire planes lie perpendicular to the magnetic field and are located at the top of the detector. The field cage produces a uniform electric field anti-parallel to the magnetic field. It is filled with gas at just above atmospheric pressure to eliminate the possibility of air entering into the field cage.

During the 2016 experimental campaign, the TPC was filled with P10 gas (90% Argon, 10% CH_4), and used to measure the collisions of Rare-Isotope (RI) beams with fixed targets located at the entrance of the field cage of the TPC. The focus of these experiments was to study central nucleus-nucleus collisions. The centrality of these collisions can be assessed by counting the number of charged particles (multiplicity) emitted in these collisions; this multiplicity generally increases as the impact parameter for the collision decreases. As these charged particles pass through the P10 gas within the field cage, they ionize molecules in the gas mixture, creating

---

[a] Corresponding author; Electronic mail: jonebarney@gmail.com
[b] Corresponding author; Electronic mail: lynch@nscl.msu.edu
[c] Corresponding author; Electronic mail: isobe@riken.jp
[d] Corresponding author; Electronic mail: murakami.tetsuya.3e@kyoto-u.ac.jp
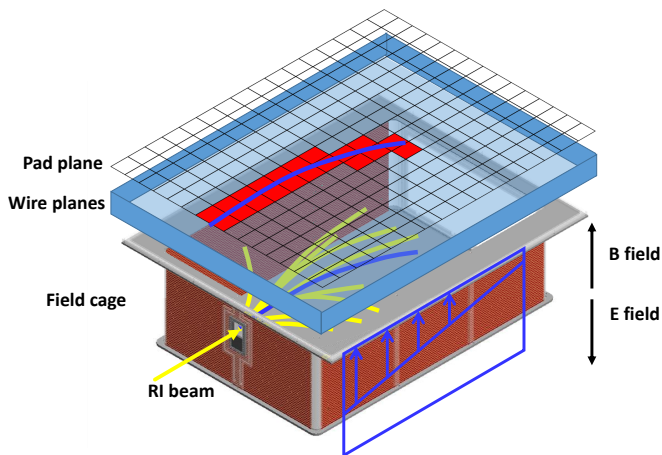[e] Corresponding author; Electronic mail: tsang@nscl.msu.edu

FIG. 1: Operation principle of the SπRIT TPC.

TABLE I: Properties of the SπRIT TPC

Pad plane area	134.4 cm × 86.4 cm
Number of pads	12,096 (112 × 108)
Pad size	1.2 cm × 0.8 cm
Drift distance	50.5 cm
Electronics sampling frequency	40 MHz
Signal shaping time	117 ns
Electronic noise	800 q_e
Gas pressure	1 atm
Typical gas composition	90% Ar + 10% CH_4
Gas gain	∼1000
Electric field	125 V/cm
Magnetic field	0.5 T
Drift velocity	5.5 cm/μs
Event rate	50-60 Hz
Typical track multiplicity	60

electron-ion pairs. The positive ions drift downward toward the cathode plate, while the electrons drift upward toward the ground wire plane. The high voltage (HV) potential between the ground and anode wire planes accelerates the drifting electrons, giving them sufficient energy to liberate additional electrons from the gas. The additional liberated electrons will also be accelerated, freeing more electrons. This sequence of ionization produces an avalanche of electrons. Thus the region between the ground and anode wire planes is known as the avalanche region. The electrons terminate on the anode plane, and the motion of the positive ions produced in the avalanche region induces an image charge on the pad plane, creating a signal large enough to be amplified and digitized by the readout electronics.

I. SπRIT TIME PROJECTION CHAMBER

Many aspects of the design of the SπRIT TPC resemble that of the EOS TPC[6], as both detectors measured heavy ion collisions in fixed target mode within a dipole magnet of similar design. The SπRIT TPC operates within the SAMURAI dipole[5], which has a magnet diameter similar to that of the HISS dipole[7] that housed the EOS TPC, but the SAMURAI dipole has a smaller usable gap of 75 cm. Table I lists some of the SπRIT TPC operating parameters.

An exploded view of the SπRIT TPC is shown in Fig. 2, with key components labeled. To facilitate the description of the TPC, we define a coordinate system of the TPC relative to the pad plane, with the origin and axis shown in Fig. 2. By convention, the z dimension lies along the beam axis. The y dimension lies along the direction of the magnetic field, which points upward and the x dimension is defined to be consistent with a right-handed Cartesian coordinate system. For clarity, directional descriptions (top, bottom, etc.) are indicated in the inset.

The top plate provides the rigid mounting surface for the readout electronics, pad plane, wire planes, target mechanism, and field cage. Unlike the EOS TPC, we position the wire planes at the top of the field cage, which is attached to the top
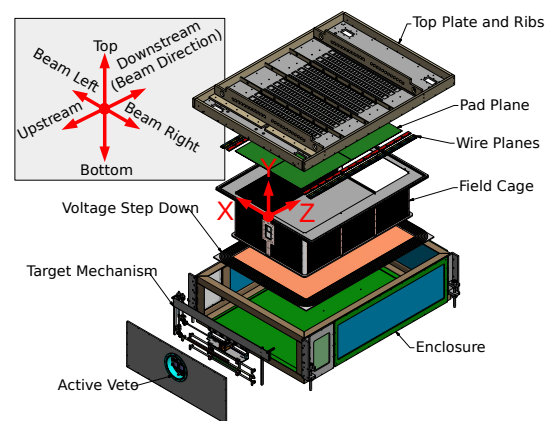

FIG. 2: Exploded view of the SπRIT TPC, with key components labeled and direction indicators in the inset.

plate. This configuration helps to protect the pad plane and wire planes from falling objects and facilitates in the convective removal of the heat generated by the TPC readout electronics located on top of the TPC. The voltage step down, which safely interfaces the high voltage of the cathode to ground, is located at the bottom of the enclosure. As discussed in more detail later, the voltage step down defines the electric field between the high voltage of the cathode with the outer enclosure, and is designed to safely allow electric fields up to 400 V/cm, much higher than would otherwise be possible. This makes it possible to use gases with lower drift velocities such as H_2 or He-CO_2 within the TPC. The first experimental campaign ran in fixed target mode, with metallic Sn target foils located 8.6 mm upstream of the entrance window of the field cage, using P10 as the counter gas.

The following subsections give detailed descriptions of various parts of the TPC identified in Fig. 2.

A. The Rigid Top Plate

The rigid top plate is made of aluminum, with a set of aluminum ribs affixed to the sides. These ribs contribute to the rigidity of the top plate, and provide support for the weight of the front end electronic modules of the Generic Electronics for TPC[8] (GET) system. The rigidity of the top plate ensures that the pad plane remains flat, and the distance from wire planes to pad plane remains fixed. The GET electronics provides 12 bit readout (4096 channels) of the pad signals. This is important for achieving the wide dynamic range in energy loss required for the scientific program of the SπRIT TPC. Both options for complete-readout of all channels and partial-readout of individual channels above specified thresholds are available. Due to the high charged particle multiplicities of the events of interest in the first experimental campaign, however, there was no advantage to use the partial-readout mode. All channels were read for each event instead. A detailed description of the implementation of the GET electronics with the SπRIT TPC is provided in Ref. 9.

B. Pad Plane and Wire Planes

The SπRIT TPC utilizes a Multi-Wire Proportional Chamber (MWPC) configuration, with an anode and ground plane defining an avalanche region which produces signals on a charge-sensitive pad plane. An additional wire plane, referred to as the gating grid, is used to control the flow of electrons into the avalanche region and to prevent the back-flow of positive ions into the larger field cage volume. The pad plane and wire planes are mounted on the bottom side of the rigid top plate, which corresponds to the top of the field cage, as shown in Fig. 2.

This choice of multi-wire gas amplification versus a GEM[10] or MICROMEGAS[11] gas amplifier has both advantages and disadvantages. One disadvantage is that wire planes require considerable labor to construct. Another is the requirement for a gating grid to prevent backstreaming of positive ions produced at the anode wires during the gas amplification process. Opening and closing this gating grid introduces deadtime. Neither disadvantage has proven problematic for the SπRIT TPC experimental program. On the other hand, there are advantages to our multi-wire gas amplification choice because its wire amplification geometry induces useful image charges over both the central pad and the adjacent pads. Using the pad distribution function and the charge deposited on adjacent pads one can determine track centroids. More importantly, since the induced charges on the neighboring pads are roughly a factor of five smaller than the charge induced in the pads directly below the track, the pad response function can be used to extend the energy loss measurement dynamic range by a factor of five With the software algorithm described in Ref. 12.

The schematic drawing at the top of Fig. 3 shows the relative positions of wires below the pad plane. The photo represents a view looking upward from below the wire planes. Fig. 4 is the side view, showing different heights of the wire
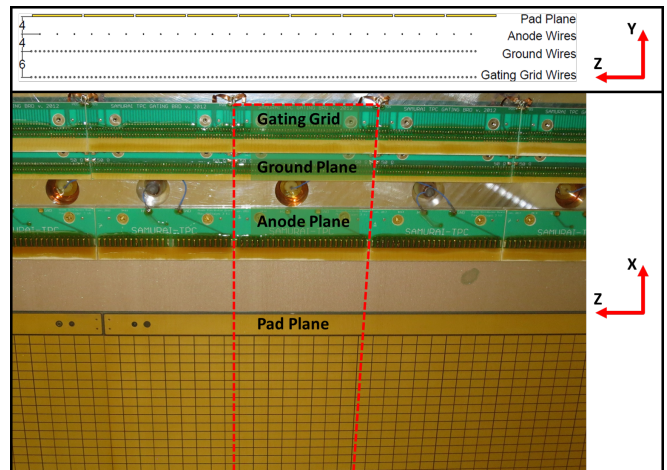

FIG. 3: Photograph of the pad plane and wire planes. The red dashed line shows the outline of a single wire plane section, which is shown schematically from the side in the top panel, with dimensions in mm.

planes. The physical properties of each wire plane are listed in Table II. The anode plane, made with 20 μm diameter gold plated tungsten wires[13], is 4 mm below the pad plane, with a pitch of 4 mm between wires. The ground plane, made with 75 μm diameter beryllium copper wires[14], is 8 mm below the pad plane, with a pitch of 1 mm between wires. The gating grid plane, made with 75 μm diameter beryllium copper wires[14], is 14 mm below the pad plane with a pitch of 1 mm between wires. The wire planes are separated into 14 sections, with each section spanning 10.4 cm along the beam axis, and stretched across the width of the pad plane. Each section contains 26 anode wires, 104 ground wires, and 104 gating grid wires. The wires are positioned to be symmetric across the center of each pad, with every third anode wire centered below a pad, and every fourth ground and gating grid wire centered below an anode wire. Fig. 3 shows the outline of a single wire plane section with a dashed line.

The ground plane is normally grounded to the TPC enclosure. We implement a switch with an option to remove this ground connection in order to pulse the ground plane. Pulsing the ground plane induces signals uniformly in the pad plane, allowing the gain and the zero offset of the pad plane electronics to be determined without using radioactive source or beams[15]. In general, the electronics behaves quite uniformly. Fig. 5 shows the distributions of the pedestals for all 12,096 channels, plotted in log scale. The RMS is found to be 5.4 ADC channels (full scale is 4096 channels) with standard deviation of 0.35 ADC channels[15].

By pulsing the ground plane with voltages ranging from 0 to 8 Volts, we can calibrate and match all 12,096 channels. The left panel of Fig. 6 shows the voltage vs. ADC channels results for all 12,096 channels. Only two channels deviate significantly from the others. Once they are calibrated to the voltage, all points (including the two outliers) collapse onto an universal calibration curve shown in the right panel. The standard deviation of the gain distribution is reduced by more

TABLE II: Wire plane properties.

Plane	Wire material	Diameter (μm)	Pitch (mm)	Distance to pad plane (mm)	Tension (N)	Total wires
Anode	Au-plated W	20	4	4	0.5	364
Ground	BeCu	75	1	8	1.2	1456
Gating	BeCu	75	1	14	1.2	1456
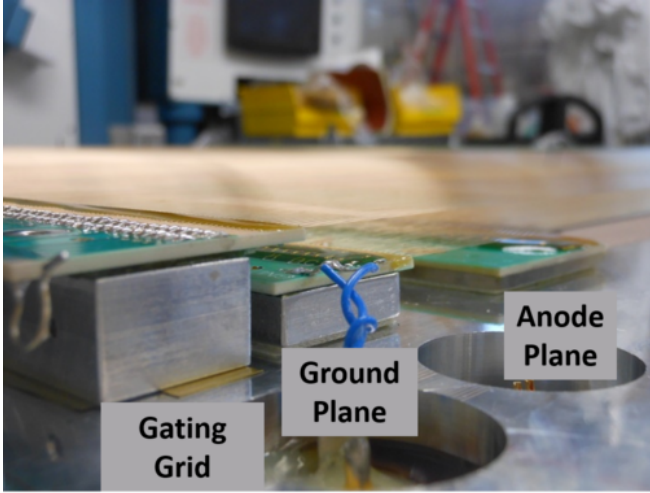
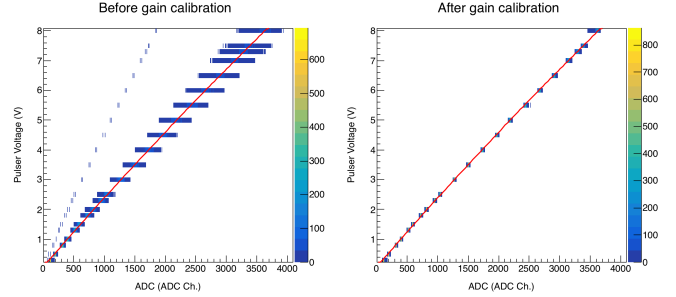FIG. 4: Photograph of the wire planes, from the side. Each plane is labeled.

FIG. 6: Distribution of the pad response to pulsed signals on the ground plane before (left) and after (right) performing gain calibration for all 12,096 channels. Reproduced from G. Jhang, PhD Dissertation, 2016, Licensed under a Creative Commons Attribution (CC BY 2.0) License

FIG. 5: Distribution of RMS variation of pedestal for all 12,096 ADC channels. Reproduced from G. Jhang, PhD Dissertation, 2016, Licensed under a Creative Commons Attribution (CC BY 2.0) License.

than a factor of 10 after the relative gain matching[15].

The amplification of charge, or gain, is described by the first Townsend coefficient α, which depends on the gas properties and electric field within the amplification region[16]. This is defined by the voltage on the anode wires, the distance between anode and pad plane, and the distance between anode plane and ground plane. The dependence of α on gas choice and

density can be determined using simulation software such as GARFIELD[17], or by comparison to measurements with similar electric fields. For the SπRIT TPC with P10 gas at atmospheric pressure and anode wires at 1460 V, the gas gain was calculated to be about 1000 using GARFIELD. The observed signals in the pad plane are compatible with these calculations. The anode wire planes are biased using two iseg EHS 8630p-F modules, mounted in an ECH 238 chassis. With these modules, we can also monitor the current in the anode wires.

The gating grid is used to prevent the amplification of charge from unwanted events which can induce background, accelerate detector aging, and add to space charge effects. Detector aging occurs when the amplification of electrons produces negative polymers from impurities in the gas. Such polymers will collect on the anode wires, increasing their effective radius, reducing the gas gain and deteriorating the performance of the TPC[18]. The amplification of electrons also produces a large number of positive ions that move away from the anode plane toward the drift region. These ions move much slower than the electrons, and can accumulate within the drift region, distorting the electric field and affecting the track reconstruction accuracy. The back-flow of these positive ions can be mitigated if they are captured on wires shortly after leaving the avalanche region. By preventing electron amplification for events which do not satisfy the physics trigger, the production of space charge and the detector aging effects are reduced. This is accomplished by the gating grid wire plane.

The capacitance of the gating grid plus biasing cables is approximately 26.5 nF. If bias is applied through a driver supply and transmission line of 50 Ohm impedance, the RC time con-

stant for discharging and opening of the gating grid would be approximately 1.3 μs. This opening time would be significant compared to the total drift time of 9.5 μs in the field cage of the TPC. Such a long opening time would cause electrons from the tracks in much of the upper part of the field cage to be deposited on the gating grid before it opens; that portion of the tracks would not be recorded as data. To address this problem, we designed a driver which charged and discharged the gating grid through a transmission lines with impedance of Z<2 ohm. With this, we opened the SπRIT TPC gating grid in approximately 350 ns. The opening and closing of the gating grid is controlled with a bipolar gating grid driver[19], developed specifically for the SπRIT TPC. The gating grid is biased by two Kikusui PMC500-0.1A power supplies, and the power to the gating grid driver is supplied using a Kikusui PMC18-3A power supply.

The pad plane defines the readout area of the TPC, and is epoxied onto the bottom surface of the top plate. It contains 12,096 gold plated pads, spanning 1.2 cm × 112 pads = 134.4 cm in the beam direction, and 0.8 cm × 108 pads = 86.4 cm in the direction perpendicular to both the beam and magnetic field. The pads are arranged in "unit cells" (shown in the top panel of Fig. 7) consisting of 63 pads each. The charge sensitive portion of each pad is 11.5 mm long and 7.5 mm wide, with a 0.5 mm gap between pads. To avoid the possibility of problems with damaged connectors on the pad plane, each unit cell is read out through two Samtec FSI-125-10-L-D-AD push-type connectors. This avoids mounting connectors with easily damaged movable parts on the circuit boards; it only requires the passive contacts of the stationary board connections that are shown in red in the top of Fig. 7. The push-type connectors are mounted on rigid Printed Circuit Boards (PCBs), which connect to a protective circuit board (known as the ZAP board) through short section of ribbon cable. The ZAP board provides both protection from large signals (such as sparks) which could damage the readout electronics, and adapts signals to the high density connectors on the Amplifier, Shaper and Amplitude to Digital converter (AsAd) board of the GET readout electronics. To reduce noise and crosstalk issues, the pad plane was constructed from four 6-layer PCBs, with the cross section shown in the bottom of Fig. 7. The typical capacitance between pads and the ground was measured to be 15 pF. Including the capacitance of the ZAP board and cable connections, the total capacitance presented to the AsAd preamp on each pad is approximately 25-30 pF. The signals from the pads were channeled to the Samtec connectors through 384 openings in the top plate. Each Samtec connector was inserted through the hole to mate with matching contacts on the back side of the pad plane circuit boards.

Due to the overall size and complexity, the pad plane was fabricated with four halogen-free G10 PCBs. Each PCB is 69.2×45.2 cm, including a small isolation area around the perimeter of the pad plane. To bond the PCBs to the pad plane while achieving a pressure tight seal, lines of Araldite 2013 epoxy were applied in two concentric rectangular patterns around each opening as shown in Fig. 8. Then the PCBs were lowered onto precision shims and held in position against the rigid top plate using a precision-machined vacuum table, en-
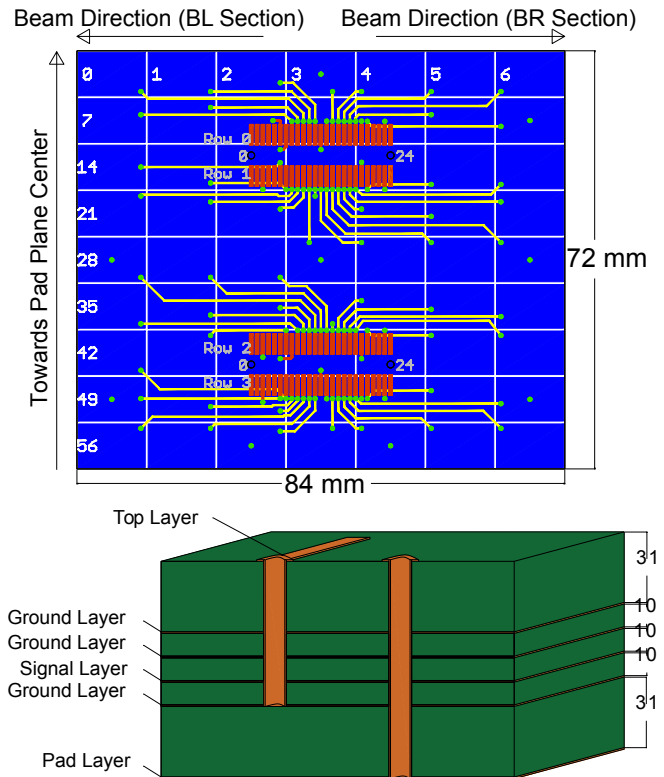

FIG. 7: The pad plane "unit cell" (top) and the pad plane layer cross section (bottom). Layer thickness indicated in mil (1 mil = 0.001"=0.0243 mm).

suring the flatness of the pad plane. After curing, the pad plane was measured with a laser alignment system, indicating uniform flatness within 125 μm. During tests with P10 gas, some leaks were detected with a combustible gas detector. Such leaks were sealed by injecting EZ-poxy through pre-existing screw holes (needed for mounting the Samtec connectors) into the space between the concentric rectangular Araldite 2013 epoxy patterns for each of the openings through which the gas was observed to be leaking. Further details of the pad plane assembly procedure can be found in Ref. 20.

C. Field cage

The field cage is the heart of the TPC, defining the detection volume in which particle tracks can be reconstructed. It is sealed by an O-ring surface at the interface between field cage and top plate, making it a gas tight detection volume. It is separated from the insulation gas volume between the field cage and the gas-tight outer enclosure; allowing the possibility of different drift and insulation gas compositions. Separating drift and insulation volumes allows the SπRIT TPC to be run as an "active target" with a pure target gas such as H_2 within the field cage inducing the reaction, and an insulation gas such as N_2 with higher dielectric strength filling the insulation volume where higher electric fields are present. Twenty-four quartz windows are installed on the walls to allow a laser

FIG. 8: Photograph of the top plate and glue pattern prior to gluing the pad plane to the top plate. The dark rectangular lines are the Araldite 2013 glue beads.
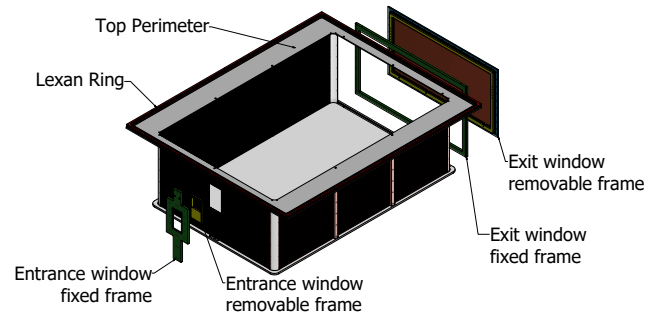

FIG. 9: Schematic view of the field cage. The entrance and exit windows are shown offset from the field cage.

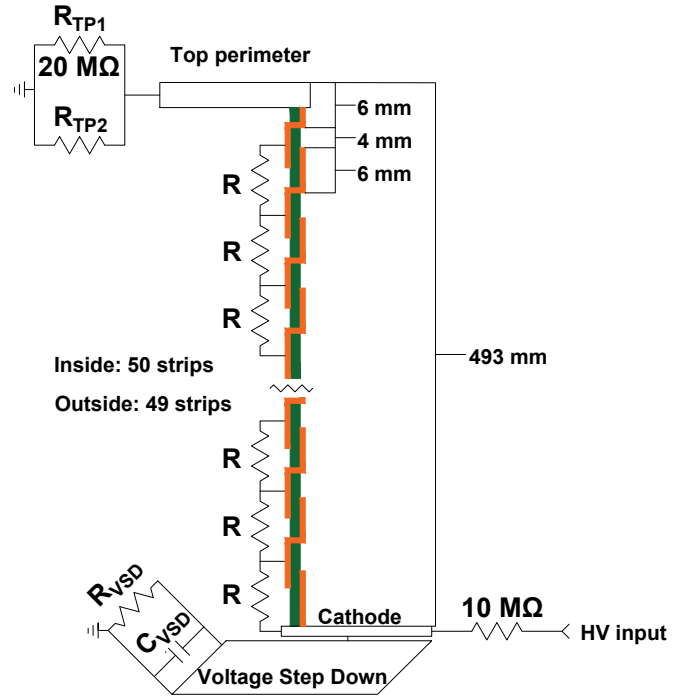FIG. 10: Schematic view of field cage resistor chain circuit.

calibration of the drift velocity within the field cage, although these laser windows have not yet been employed for that purpose.

A drawing of the field cage is shown in Fig. 9, with the windows and frames offset from the walls. It has interior dimensions of 145 cm in length, 97 cm in width, and the distance between cathode and pad plane is 51.3 cm. The upstream wall and two side walls of the field cage are made with 1.6 mm thick 2-layer G-10 PCBs, which have a precise uniform pattern of copper strips on the inside and outside, forming the equipotential strips that define the electric field. Each side wall is made with 3 PCBs, which are aligned and joined together using polycarbonate bars. The upstream wall is made with 2 PCBs, with a polycarbonate window frame in the middle. Both the upstream and downstream windows are removable to facilitate repair or replacement. The upstream entrance window is 5.73 cm wide by 7 cm tall, and made of 4 μm thick poly p-phenylene terephthalamide (PPTA). The exit window, made of 125 μm thick polyamide, is 80.8 cm wide by 38.9 cm tall and forms the entire downstream wall of the field cage. Aluminum strips are evaporated onto the windows to align with the copper strips on the PCBs. The entrance and exit windows are much thinner than the field cage walls, allowing particles to enter and exit the field cage with minimal energy loss. For example, a 50 MeV proton would lose 7keV in the entrance window and 200 keV in the exit window.

The four corners are formed with rounded G-10, eliminating sharp corners in the geometry, which can cause spark formation. The window frames and rounded corners have equipotential strips sprayed with conductive paint. For this and other equipotential surfaces formed with conductive paint, we used Parker Cho-shield 599, which is a two component, copper filled, conductive epoxy paint formulated to provide electromagnetic interference shielding and electrical grounding on insulating surfaces.

Equipotential strips on the walls and windows define an electric field between the cathode plate, the top perimeter and the gating grid. The 6 mm equipotential strips both on the inside and outside the field cage are spaced from the cathode to the top perimeter with 1 cm pitch, with sequential strips connected across the 4 mm gap by resistors. The overlapping structure of strips on both sides of the PCBs was chosen to effectively shield the pad plane from external noise. The transverse components of the electric field decay as $e^{-2\pi t/\Delta}$, where t is the distance from the wall and Δ is the pitch of the strips[16]. At a distance of 1 cm away from the field cage wall, these components of the electric field have been reduced by a factor of about 10^{-3}. The field cage produces a uniform electric field that is directed downward toward the cathode. The pad plane sits in a sufficiently uniform region that is 5 cm away from the field cage walls on all sides except for the front wall. In this case, any influence the non-uniform field has on
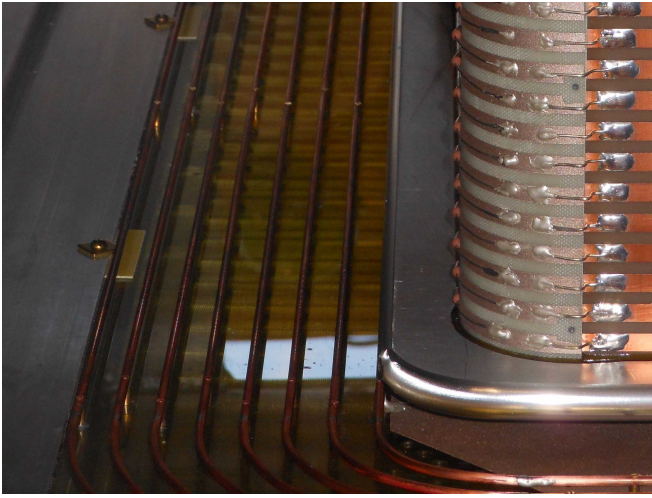
FIG. 11: Field cage and voltage step down.

electrons very close to the front wall are removed by cutting out that region in the analysis software.

There are 50 strips on the inside of the field cage, and 49 on the outside. The resistor chain circuit layout is shown in Fig. 10, with 49 resistors with resistance R=5 MΩ, as well as R_{VSD}=700 MΩ, and R_{TP2}=19.77 MΩ. The capacitance C_{VSD}=4 nF in the circuit is dictated by the thickness and area of the voltage step down. Together with the field cage resistor chain circuit, the voltage step down configuration shown in Fig. 10 effectively filters out oscillatory noise from the HV supply. High Voltage is applied to the cathode, and the strength of the electric field is adjusted by varying the cathode voltage. For the SπRIT experiments of 2016, the cathode voltage was set at -6700 V, providing electric field of 124.7 V/cm. The bias for the cathode was provided using a rack-mounted Bertan Series 205B HV Power Supply.

The field cage is secured from the top. The cathode, which forms the bottom of the field cage, is made with an aluminum honeycomb plate to minimize its weight. A lightweight cathode minimizes stress on the field cage walls, and reduces the propensity of the cathode to deform. Below the cathode, a custom made voltage step down assembly is used to define and control the electric fields associated with the large voltage difference between the cathode and the outer enclosure.

The voltage step down is built into the bottom plate of the enclosure, and consists of 8 concentric copper loops mounted on a polycarbonate base. One corner of the voltage step down, field cage and cathode is shown in Fig. 11. A conductive surface immediately below the cathode is formed by spray-painting Cho-shield 599 on the polycarbonate base. This conductive surface is electrically connected to the cathode through spring contacts, and to the innermost copper ring of the voltage step down. Each sequentially larger copper ring is connected in series to this innermost ring by 100 MΩ resistors. The outermost copper ring is grounded to the enclosure.

During the first experimental campaign, the field cage was filled with P10 gas, which is commonly used for proportional chambers and TPCs such as the EOS TPC and the STAR TPC.

The gas was bred to the TPC with a flow rate of 1 L/min. Gas flow was maintained through the field cage via a gas inlet near the upstream end of the cathode and a gas outlet at the top near the downstream end of the pad plane. Gas exiting the field cage was then transmitted by a gas line to the insulation volume and vented from the enclosure through a bubbler filled with 1 cm of mineral oil. This flow system maintained the gas pressure just above atmospheric pressure and allowed the gas volume to be efficiently purged of electronegative gases throughout our measurements. The O_2 level was monitored and maintained between 50–70 ppm during the experiment. The dew-point for the water contaminant in the counter gas was also monitored and controlled so that it remained between -37°C and -34°C, corresponding to 170–250 ppm of H_2O. The drift velocity of electrons in the gas[21] depends mainly on the ratio of electric field to pressure, E/p. Atmospheric pressure was continuously monitored. From this we determined the typical value of E/p to be 0.167 V/cm/Torr. At this field, P10 is predicted to have a drift velocity of 5.5 cm/μs according to MAGBOLTZ[22] simulation. During the first campaign of physics measurements, the electron drift velocity was measured to be 5.52± 0.02 cm/μs.

D. Target Mechanism

Solid metallic targets form equipotential surfaces that would complicate the transport of electrons from tracks near the target if placed within the drift volume of the TPC. Since most reaction products of a nucleus-nucleus collision in fixed target mode are emitted at laboratory angles less than 90°, placing the target just upstream of the field cage provides reasonable detection efficiencies for the particles of interest. Therefore, targets are mounted on a target ladder, located outside the field cage, near the entrance window, as shown in Fig. 12. The target ladder has five positions, with three targets mounted on standoffs. These standoffs are necessary to bring the targets as close as possible to the entrance window (which is 3 mm upstream of the pad plane origin), thereby facilitating minimum acceptance of 73 degrees in polar angle in the lab frame. The target ladder must be able to move along the z-axis to bring the target ladder toward the entrance window, and away from the entrance window prior to moving along the x-axis to change targets. These motions are actuated via drive mechanisms from outside the magnetic field and the target positions are calibrated using linear potentiometers. The motion to change target and place it at the correct position is controlled through rotary motion using non-magnetic lead screws. For motion along the x-axis, 4 gear pairs are used, and for motion along the z-axis, 5 gear pairs are used. The motion is patched through the top plate using commercial rotary O-ring seals for remote control.

E. TPC Enclosure

The TPC provides a gas-tight volume around the field cage, sealed at the top by the rigid top plate. The voltage step down
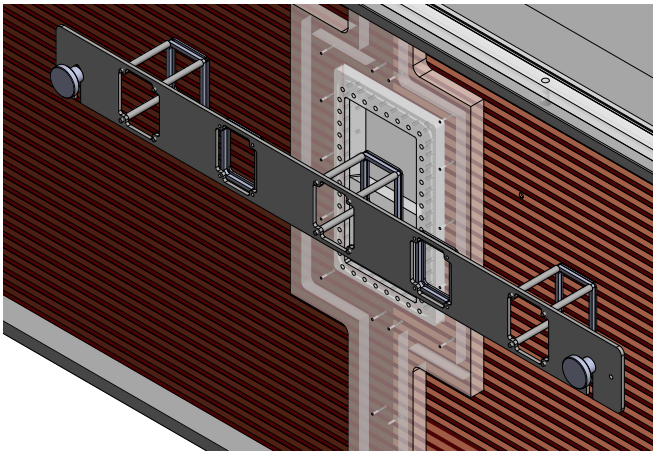
FIG. 12: Location of target ladder with respect to field cage.

FIG. 13: TPC enclosure design, without top plate.

is mounted to the bottom of the enclosure. The upstream side panel is made of 12.7 mm thick aluminum, with a cutout for an entrance window. An Active Veto detector array[23] indicated in Fig. 2 was installed in this cutout, with a 4 μm thick Mylar window. Near the upstream side panels, there are small plastic windows on the beam left and right sides that provide an unobstructed view of the target motion. Thin aluminum windows (0.95 mm in thickness) cover most of the beam left, beam right and downstream sides of the enclosure. Protons with energy as low as 21 MeV can penetrate through the Al window and the 1.6 mm G10 wall. Thus, the thin enclosure windows and field cage walls allow most of the light charged particles to pass through the walls to the Kyoto[24] and Katana[25] scintillator trigger arrays that are located along the side and downstream walls of the enclosure. The enclosure is shown in Fig. 13, with panels and windows labeled.

In addition to the enclosure itself, a versatile motion chassis was constructed to enable the enclosure body and the top plate to be easily and accurately manipulated. The motion chassis served as a support for the top plate when the pad plane and wire planes were constructed. It was designed to allow the top plate to be rotated 90 degrees to pass through narrow doors and to be inverted as shown in Fig. 14 where the top plate and attached field cage are rotated for insertion into the enclosure. When attached to the TPC itself, it allows the TPC to be easily manipulated during assembly, storage and shipping.

II. SπRIT TPC PERFORMANCE

Each component of the SπRIT TPC described above worked as designed. After assembly of all the component parts at the Michigan State University, the TPC was shipped by air to RIKEN, Japan, in 2013 where the GET electronics were installed. Performance of the SπRIT TPC GET electronics is detailed in Ref. 9. The SπRIT TPC was commissioned first without magnetic field in 2015, providing critical tests of the TPC and trigger detectors[26]. In 2016, the SπRIT TPC was installed inside the SAMURAI spectrometer[5] at the RIKEN Radioactive Isotope Beam Factory (RIBF)[27]. A campaign of
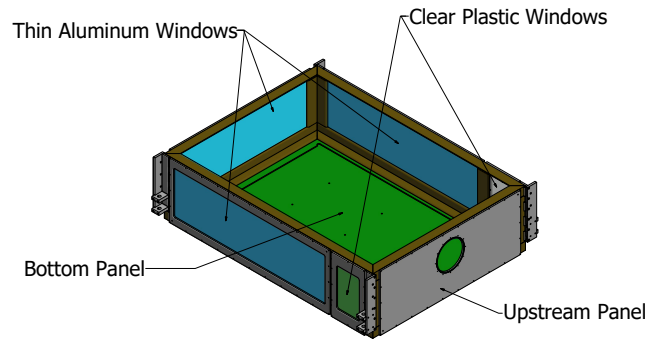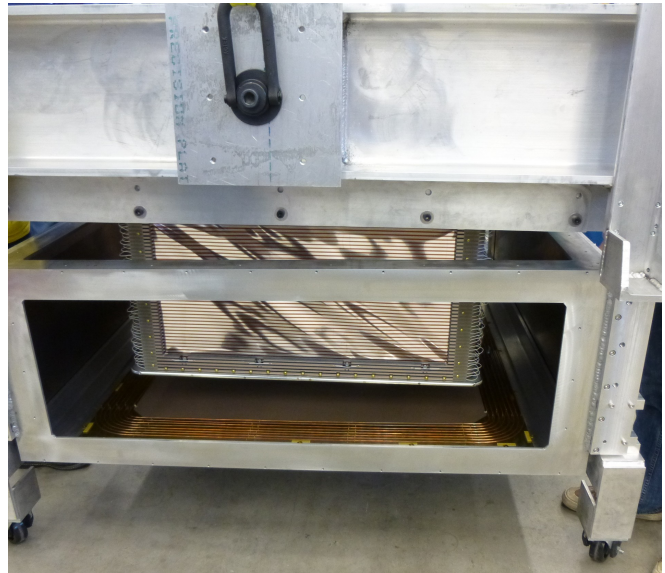

FIG. 14: Motion chassis attached to enclosure allowing the TPC to be supported and rotated.

experiments impinging neutron-rich Sn beams on isotopically enriched Sn targets was successfully carried out[3,4].

As with all modern complicated detectors, specialized software is needed to analyze the data taken with the detector. SπRITROOT is the tracking software developed specifically for the SπRIT TPC[28] to disentangle and identify all the particle tracks. It also contains all the software improvement developed to optimize the TPC performance in heavy ion collisions[9,12,19,25,26,28,29].

A. Cosmic ray Events

The SπRIT TPC detection and tracking abilities were tested with cosmic rays. During this test the TPC was installed in the SAMURAI spectrometer at 0.5 T. Its data acquisition is triggered by the Kyoto Multiplicity Array[24] detecting a signal in its beam left and beam right array. The Kyoto Multiplicity array consists of 60 plastic scintillator bars, each with
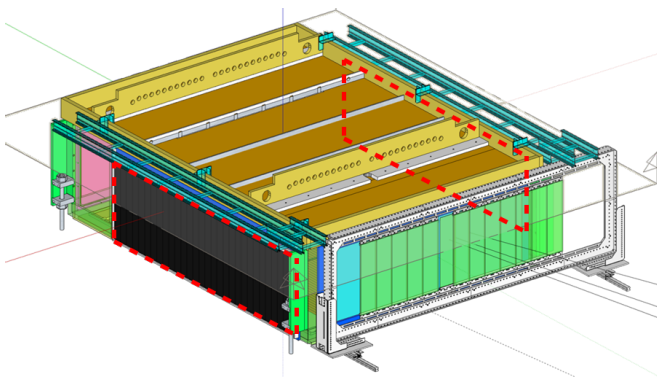
FIG. 15: TPC with the two-panel Kyoto Multiplicity Array mounted. Only one panel, in black and outlined with red dashed line, is visible in the figure. The other panel is on the opposite side of the TPC, with the outline showing its relative location. Reproduced with permission from M. Kaneko et al., RIKEN APR 50, 172 (2017). Copyright 2017, RIKEN Nishina Center for Accelerator-Based Science.
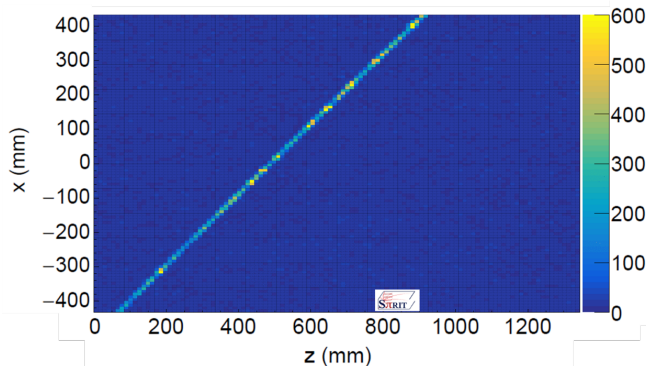

FIG. 17: A cosmic shower event recorded in the SπRIT TPC.

FIG. 16: A cosmic ray recorded in the SπRIT TPC pad-plane, shown from above.

FIG. 18: Typical noise level of pads within the unit cell, with noise level in ADC channels. The orientation of the pads matches that of Fig. 7.

dimensions $450 \times 50 \times 10$ mm^3. These bars are split into two arrays of 30 bars each, which are placed just outside the thin aluminum windows on the beam left and right sides of the TPC, as shown in Fig. 15. Each bar was read out by a Multi Pixel Photon Counter whose output was processed by a VME EASIROC board which provided a multiplicity output to the trigger system[24].

An example of an event containing one cosmic ray entering the TPC through one half of the Kyoto array and exiting the TPC through the other half of the Kyoto array is shown in Fig. 16. In this figure, the pad plane is shown, with each pad forming a pixel. Occasionally, a cosmic array will interact with material in the TPC and produce a shower of particles, as shown in Fig. 17. More images of the cosmic rays and showers can be found in Ref. 30.

The cosmic ray events are ideal to study the response of the TPC to minimum ionizing particles and to perform a measurement of the noise level of the TPC readout, since many pads will have no hits. The average noise level was calculate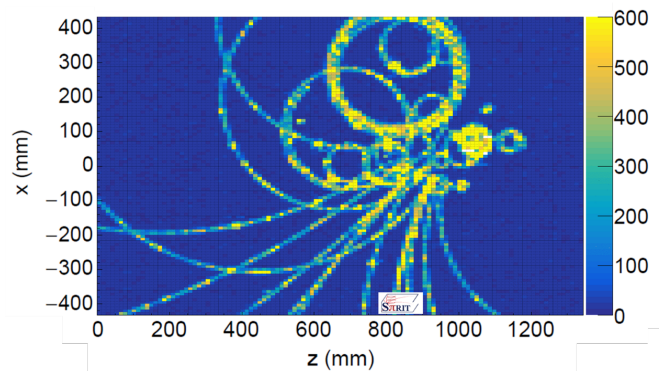d for each empty pad by taking the maximum deviation from the pedestal value. This is done for 1456 cosmic events collected within a 4 hour period. The noise level clusters in a pattern of unit cells. The average noise level for a unit cell with 7x9=63 pads is shown in Fig. 18, with the color scale given in Analog-to-Digital-Conversion (ADC) channels, with 1 ADC channel ≈ 200 q_e. The typical noise level is between 4-5 ADC channels, with a single pad of the unit cell (consisting of 7x9=63 pads) having a noise level between 5.5-6 ADC channels. These noise values are largely consistent with the noise levels expected for the GET system when the input is attached to a capacitance of approximately 25-30 pF, which is typical of our setup.

B. Nuclear Reaction Events

The main function of the TPC is to identify the particles produced in heavy ion collisions and measure their momentum. Due to the large dynamic range we employ, most of the particle tracks are not perfect. Below we briefly discuss the innovative optimizations used to better identify charged particles in the TPC that allows accurate determination of their momentum. Most of the technical details and novel analysis

techniques developed for the SπRIT TPC described here have been published[9,12,19,25,26,28,29]. The performance of the TPC is verified by the excellent particle identification from pions to Lithium isotopes shown at the end of this section.

Fig. 19 shows a typical Sn+Sn collision event recorded by the TPC pad-plane, viewed from above in the top panel, and viewed from the side in the bottom panel. This event illustrates that positioning the target immediately upstream of the field cage allows most particles to enter the detection volume. This is especially true for collisions of nearly symmetric systems as in the Sn+Sn collisions. We have 100% coverage for center of mass polar angle, $\theta_{c.m.} < 90°$. Quality of tracks are typically very good in the x-z plane due to the longer track lengths, but for particles detected in the up-down position, the tracks are shorter and the quality are inferior. To ensure good quality of the data especially for pions, we analyze data at azimuthal angles $-40° < \phi < 25° \cup 160° < \phi < 210°$, where the particle momenta are mainly perpendicular to the magnetic field. Since particle emissions are isotopic in ϕ, geometric efficiencies can be easily corrected.

A number of features can be observed in this event in Fig. 19. First, the region near the target, marked with a red half-ellipse, has a high track density, saturating the electronics for many pads. It is impossible to accurately measure the individual tracks in this region and is excluded from analysis. Second, the tracks are broken in the vertical direction, as can be seen in the bottom panel between -30 and -20 timebuckets. This is due to the gating grid, which takes 350–400 ns to open and settle down. Above this region, there are portions of these tracks that correspond to the ionization of particles that physically penetrate through the gating grid and ionize the gas above the gating grid. Third, there are two regions run at reduced gain, between z=1084–1188 mm and z=1296–1344 mm.

Finally, there are a number of blue pads in the vicinity of the beam trajectory where regions of high ionization density are expected. These pads are "dead" and provide no useful information in this event. The blue color corresponds to the noise level of the shaper output in the readout electronics. These dead pads are most frequently caused by very energetic delta electrons from an unreacted beam particle that passed through the TPC prior to the recorded event. These electrons spiral upward along the magnetic field lines through the gating grid while it is closed. High amounts of charge from multiple particles on a pad will also saturate the charge sensitive amplifier, causing the pad to be insensitive to any further signals for a period of time proportional to the amount of incident charge. The recovery time for these channels is governed by the preamp fall time of approximately 50 μs. After 50 μs the preamps recover and these electronic channels are available to take data on the next event. Further exploration of this phenomenon is provided in Ref. 9.

The maximum energy loss which can be measured in a single pad is limited by the saturation limit for the charge sensitive amplifier. By incorporating information from nearby pads, however, energy loss can be determined even for tracks which saturate the electronics. The software method described in details in Ref. 12 was developed and implemented
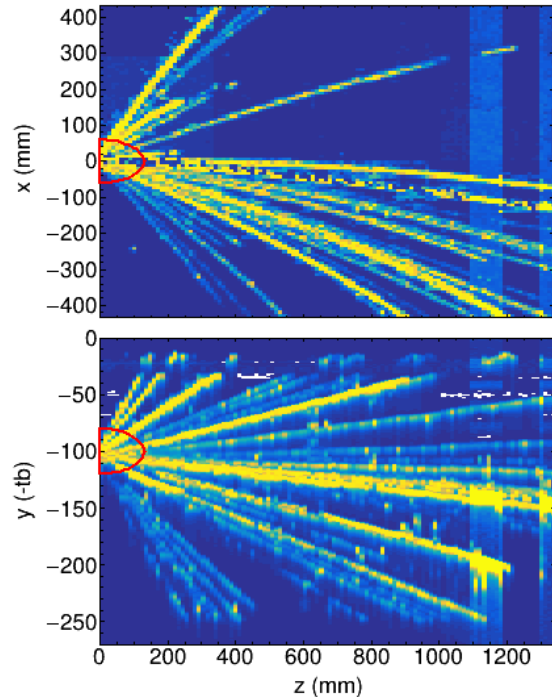

FIG. 19: A typical event in the TPC, shown from (top) above, and (bottom) the side. The view from above corresponds to the pad plane, with each pixel representing a pad, and the side view showing the time measurement, with each pixel representing a pad length and timebucket width.

in SπRITROOT. The two regions of lowered gain were used to calibrate and verify this method, as most tracks that saturate the high gain regions do not saturate the low gain region. The saturation correction is key to identifying particles with dE/dx >2 MeV/mm (corresponding to 430 ADC/mm) in Fig. 20. Without corrections, these tracks would provide no information and the PID lines with dE/dx greater than 400 ADC/mm are distorted[12].

It was observed that tracks in boundary regions, directly near any of the field cage edges, including the cathode and gating grid boundaries, exhibit sharp deflection, which negatively affects track reconstruction. They were excluded from analysis. By excluding the boundary and high density regions, we are able to achieve excellent reconstruction of individual tracks, as well as the reconstruction of event characteristics, including the event vertex[28,31].

Due to the thin entrance window and field cage walls, non-interacting beam particles also pass directly through the detection volume. These beam particles create slowly drifting positive ions that form a space charge distribution that distorts the drift field. We have successfully modeled these distortions and applied an inverse-map correction as described in Ref. 29, allowing the proper determination of track trajectories which is the key to accurate measurement of the momentum of the particles. The trajectory of each track is determined by the centroid of a cluster of pads; typically, there are two or more
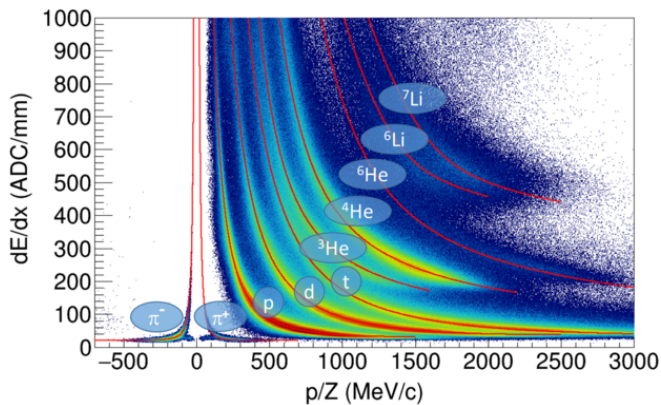
FIG. 20: PID plot for combined ^{132}Sn + ^{124}Sn and ^{108}Sn + ^{112}Sn systems. Expected PID lines are drawn up to Lithium isotopes. The formula converting ADC channel to Kev is : E (keV) = 0.00455*(ADC+8.3).

pads in the *x* and *z* directions with signals well above the noise for most points on the trajectory, allowing the track centroid to be determined with typical standard deviations of 0.65, 0.71, 0.56 mm in x,y,z direction, respectively[28]. This is achieved even with pads that have lateral dimensions of the order of 1 cm. Energy loss in the target, entrance windows and counter gas is taken into account in the determination of the momentum of a particle. The transverse momentum resolution is determined to be 1.5% for deuteron and 2% for tritons around 1700 MeV/c[28].

Finally, the Particle IDentification (PID) is made by plotting the magnetic rigidity $B\rho$ and energy loss dE/dx of each track. Fig. 20 shows the PID from the combined ^{132}Sn + ^{124}Sn and the ^{108}Sn + ^{112}Sn systems. Both positive and negative pions are clearly visible, as well as hydrogen, helium, and lithium isotopes. Electron and positron lines from π^0 decays are present, diverging from the pion lines at p/Z≈100 MeV/c, but are not labeled in the figure. The low noise to signal ratio of the electronics allows clear PID line separation. The PID resolution varies with particles, worsening with A and Z as well as the energy of the particles. Above A=2, the background contributes significantly. For the Z=1 isotopes where we have done extensive analysis, the standard deviation of the mass resolutions are ≈ 6%.

III. CONCLUSIONS

The SπRIT TPC has been constructed, placed within the SAMURAI spectrometer and used successfully in experiments with rare isotope beams at RIBF. A description of key components of the TPC is provided in this article. The electronic noise levels were sufficiently low to resolve minimum ionizing particles such as pions and with a sufficient gain to resolve Li isotopes. The particle tracking combined with the corrections for space charge allow precise momentum measurement[12,29]. Solutions to the technical challenges of building the TPC prove that the SpRIT TPC is able to achieve

the dynamical range requirements for measurements of central collisions of heavy ion beams with anticipated energy ranges of 200–500 AMeV. Its performance is demonstrated in the successful analysis and recent publication of the TPC data obtained in an experimental campaign to measure pions produced in the central collisions of rare Sn beams on Sn targets at 270 AMeV[3,4].

DATA AVAILABILITY

The data that support the findings of this study are available from the corresponding author upon reasonable request.

REFERENCES

[1]C. Horowitz, E. Brown, Y. Kim, W. Lynch, R. Michaels, A. Ono, J. Piekarewicz, M. Tsang, and H. Wolter, "A way forward in the study of the symmetry energy: experiment, theory, and observation," Journal of Physics G: Nuclear and Particle Physics **41**, 093001 (2014).

[2]R. Shane, A. B. McIntosh, T. Isobe, W. G. Lynch, H. Baba, J. Barney, Z. Chajecki, M. Chartier, J. Estee, M. Famiano, B. Hong, K. Ieki, G. Jhang, R. Lemmon, F. Lu, T. Murakami, N. Nakatsuka, M. Nishimura, R. Olsen, W. Powell, H. Sakurai, A. Taketani, S. Tangwancharoen, M. B. Tsang, T. Usukura, R. Wang, S. J. Yennello, and J. Yurkon, "SπRIT: A time-projection chamber for symmetry-energy studies," Nucl. Inst. Meth. A **784**, 513–517 (2015).

[3]G. Jhang, J. Estee, J. Barney, G. Cerizza, M. Kaneko, J. Lee, W. Lynch, T. Isobe, M. Kurata-Nishimura, T. Murakami, C. Tsang, M. Tsang,

R. Wang, D. Ahn, L. Atar, T. Aumann, H. Baba, K. Boretzky, J. Brzychczyk, N. Chiga, N. Fukuda, I. Gasparic, B. Hong, A. Horvat, K. Ieki, N. Inabe, Y. Kim, T. Kobayashi, Y. Kondo, P. Lasko, H. Lee, Y. Leifels, J. Łukasik, J. Manfredi, A. McIntosh, P. Morfouace, T. Nakamura, N. Nakatsuka, S. Nishimura, R. Olsen, H. Otsu, P. Pawłowski, K. Pelczar, D. Rossi, H. Sakurai, C. Santamaria, H. Sato, H. Scheit, R. Shane, Y. Shimizu, H. Simon, A. Snoch, A. Sochocka, Z. Sosin, T. Sumikama, H. Suzuki, D. Suzuki, H. Takeda, S. Tangwancharoen, H. Toernqvist, Y. Togano, Z. Xiao, S. Yennello, J. Yurkon, Y. Zhang, M. Colonna, D. Cozma, P. Danielewicz, H. Elfner, N. Ikeno, C. M. Ko, J. Mohs, D. Oliinychenko, A. Ono, J. Su, Y. J. Wang, H. Wolter, J. Xu, Y.-X. Zhang, and Z. Zhang, "Symmetry energy investigation with pion production from Sn+Sn systems," Physics Letters B **813**, 136016 (2021).

[4]J. Estee, W. G. Lynch, C. Y. Tsang, J. Barney, G. Jhang, M. B. Tsang, R. Wang, M. Kaneko, J. W. Lee, T. Isobe, M. Kurata-Nishimura, T. Murakami, D. S. Ahn, L. Atar, T. Aumann, H. Baba, K. Boretzky, J. Brzychczyk, G. Cerizza, N. Chiga, N. Fukuda, I. Gasparic, B. Hong, A. Horvat, K. Ieki, N. Inabe, Y. J. Kim, T. Kobayashi, Y. Kondo, P. Lasko, H. S. Lee, Y. Leifels, J. Łukasik, J. Manfredi, A. B. McIntosh, P. Morfouace, T. Nakamura, N. Nakatsuka, S. Nishimura, H. Otsu, P. Pawłowski, K. Pelczar, D. Rossi, H. Sakurai, C. Santamaria, H. Sato, H. Scheit, R. Shane, Y. Shimizu, H. Simon, A. Snoch, A. Sochocka, T. Sumikama, H. Suzuki, D. Suzuki, H. Takeda, S. Tangwancharoen, H. Toernqvist, Y. Togano, Z. G. Xiao, S. J. Yennello, Y. Zhang, and M. D. Cozma (SπRIT Collaboration), "Probing the symmetry energy with the spectral pion ratio," Phys. Rev. Lett. **126**, 162701 (2021).

[5]T. Kobayashi, N. Chiga, T. Isobe, Y. Kondo, T. Kubo, K. Kusaka, T.Motobayashi, T.Nakamura, J.Ohnishi, H.Okuno, H.Otsu, T.Sako, H.Sato, Y.Shimizu, K.Sekiguchi, K.Takahashi, R.Tanaka, and K.Yoneda, "SAMURAI spectrometer for RI beam experiments," Nucl. Inst. Meth. B **317**, 294–304 (2013).

[6]G. Rai, A. Arthur, F. Bieser, C. W. Harnden, R. Jones, S. Kleinfelder, K. Lee, H. S. Matis, M. Nakamura, C. McParland, D. Nesbitt, G. Odyniec, D. Olson, H. G. Pugh, H. G. Ritter, T. J. M. Symons, H. Wieman, M. Wright, R. Wright, and A. Rudge, "A TPC detector for the study of high multiplicity heavy ion collisions," IEEE Transactions on Nuclear Science **37**, 56–64 (1990).

[7]R. Wolgast, V. Fletcher, A. Kennedy, and Y. Kajiyama, "A large superconducting dipole magnet for the heavy ion spectrometer system (HISS)," IEEE Transactions on Magnetics **17**, 195–198 (1981).

[8]E. Pollacco, G. Grinyer, F. Abu-Nimeh, T. Ahn, S. Anvar, A. Arokiaraj, Y. Ayyad, H. Baba, M. Babo, P. Baron, D. Bazin, S. Beceiro-Novo, C. Belkhiria, M. Blaizot, B. Blank, J. Bradt, G. Cardella, L. Carpenter, S. Ceruti, E. D. Filippo, E. Delagnes, S. D. Luca, H. D. Witte, F. Druillole, B. Duclos, F. Favela, A. Fritsch, J. Giovinazzo, C. Gueye, T. Isobe, P. Hellmuth, C. Huss, B. Lachacinski, A. Laffoley, G. Lebertre, L. Legeard, W. Lynch, T. Marchi, L. Martina, C. Maugeais, W. Mittig, L. Nalpas, E. Pagano, J. Pancin, O. Poleshchuk, J. Pedroza, J. Pibernat, S. Primault, R. Raabe, B. Raine, A. Rebii, M. Renaud, T. Roger, P. Roussel-Chomaz, P. Russotto, G. Saccà, F. Saillant, P. Sizun, D. Suzuki, J. Swartz, A. Tizon, N. Usher, G. Wittwer, and J. Yang, "GET: A generic electronics system for TPCs and nuclear physics instrumentation," Nuclear Instruments and Methods in Physics Research Section A: Accelerators, Spectrometers, Detectors and Associated Equipment **887**, 81 – 93 (2018).

[9]T. Isobe, G. Jhang, H. Baba, J. Barney, P. Baron, G. Cerizza, J. Estee, M. Kaneko, M. Kurata-Nishimura, J. Lee, W. Lynch, T. Murakami, N. Nakatsuka, E. Pollacco, W. Powell, H. Sakurai, C. Santamaria, D. Suzuki, S. Tangwancharoen, and M. Tsang, "Application of the Generic Electronics for Time Projection Chamber (GET) readout system for heavy Radioactive isotope collision experiments," Nuclear Instruments and Methods in Physics Research Section A: Accelerators, Spectrometers, Detectors and Associated Equipment **899**, 43 – 48 (2018).

[10]F. Sauli, "Gem: A new concept for electron amplification in gas detectors," Nuclear Instruments and Methods in Physics Research Section A: Accelerators, Spectrometers, Detectors and Associated Equipment **386**, 531 (1997).

[11]Y. Giomataris, P. Rebourgeard, J. P. Robert, and G. Charpak, "Micromegas: A high-granularity position-sensitive gaseous detector for high particle-flux," Nuclear Instruments and Methods in Physics Research Section A: Accelerators, Spectrometers, Detectors and Associated Equipment **376**, 29 (1996).

[12]J. Estee, W. Lynch, J. Barney, G. Cerizza, G. Jhang, J. Lee, R. Wang, T. Isobe, M. Kaneko, M. Kurata-Nishimura, T. Murakami, R. Shane, S. Tangwancharoen, C. Tsang, M. Tsang, B. Hong, P. Lasko, J. Łukasik, A. McIntosh, P. Pawłowski, K. Pelczar, H. Sakurai, C. Santamaria, D. Suzuki, S. Yennello, and Y. Zhang, "Extending the dynamic range of electronics in a time projection chamber," Nuclear Instruments and Methods in Physics Research Section A: Accelerators, Spectrometers, Detectors and Associated Equipment **944**, 162509 (2019).

[13]"Luma Metall website," https://luma-metall.com/, accessed on October 10, 2019.

[14]"California Fine Wire Co. website," https://www.calfinewire.com/index.html, accessed on October 10, 2019.

[15]G. Jhang, "Performance of the SπRIT TPC for the nuclear physics experiment at RIBF," Korea University Library (2016).

[16]W. Blum, W. Riegler, and L. Rolandi, "Particle detection with drift chambers," (Springer Science & Business Media, 2008) Chap. 8.4, pp. 132–133.

[17]R. Veenhof, "GARFIELD, recent developments," Nuclear Instruments and Methods in Physics Research Section A: Accelerators, Spectrometers, Detectors and Associated Equipment **419**, 726–730 (1998).

[18]V. Blinov, I. Popkov, and A. Yushkov, "Aging measurements in wire chambers," Nuclear Instruments and Methods in Physics Research Section A: Accelerators, Spectrometers, Detectors and Associated Equipment **515**, 95 – 107 (2003), proceedings of the International Workshop on Aging Phenomena in Gaseous Detectors.

[19]S. Tangwancharoen, W. G. Lynch, J. Barney, J. Estee, R. Shane, M. B. Tsang, Y. Zhang, T. Isobe, M. Kurata-Nishimura, T. Murakami, Z. Xiao, Y. F. Zhang, and the SπRIT collaboration, "A gating grid driver for time-projection chambers," Nucl. Inst. Meth. A **853**, 44–52 (2017).

[20]J. Barney, "Charged pion emission from 112sn + 124sn and 124sn + 112sn reactions with the sπrit time projection chamber," Michigan State University Library (2019), https://d.lib.msu.edu/etd/48169/datastream/OBJ/View/.

[21]A. Andronic, S. Biagi, P. Braun-Munzinger, C. Garabatos, and G. Tsiledakis, "Drift velocity and gain in argon- and xenon-based mixtures," Nuclear Instruments and Methods in Physics Research Section A: Accelerators, Spectrometers, Detectors and Associated Equipment **523**, 302 – 308 (2004).

[22]S. Biagi, "Magboltz-transport of electrons in gas mixtures," CERN program library (2000).

[23]Y. Zhang, J. Barney, M. Kaneko, M. Kurata-Nishimura, P. Lasko, J. Łukasik, P. Pawłowski, X. Xiao, et al., "The Veto Collimator for the SπRIT-TPC," RIKEN Accel. Prog. Rep. **50**, 170 (2017).

[24]M. Kaneko, T. Murakami, T. Isobe, M. Kurata-Nishimura, W. G. Lynch, M. B. Tsang, J. Barney, J. Estee, G. Cerizza, C. Santamaria, et al., "Kyoto Multiplicity Array for the SπRIT experiment," RIKEN Accel. Prog. Rep. **50**, 172 (2017).

[25]P. Lasko, M. Adamczyk, J. Brzychczyk, P. Hirnyk, J. Łukasik, P. Pawłowski, K. Pelczar, A. Snoch, A. Sochock, Z. Sosin, J. Barney, G. Cerizza, J. Estee, T. Isobe, G. Jhang, M. Kaneko, M. Kurata-Nishimura, W. G. Lynch, T. Murakami, C. Santamaria, M. B. Tsang, and Y. Zhang, "KATANA - A charge-sensitive triggering system for the SπRIT experiment," Nucl. Inst. Meth. A **856**, 92–98 (2017).

[26]G. Jhang, J. Barney, J. Estee, T. Isobe, M. Kaneko, M. Kurata-Nishimura, G. Cerizza, C. Santamaria, J. W. Lee, P. Lasko, J. Łukasik, W. G. Lynch, A. B. McIntosh, T. Murakami, P. Pawłowski, R. Shane, S. Tangwancharoen, M. B. Tsang, H. Baba, B. Hong, Y. J. Kim, H. S. Lee, H. Otsu, K. Pelczar, H. Sakurai, D. Suzuki, Z. Xiao, S. J. Yennello, Y. Zhang, and the SπRIT Collaboration, "Beam Commissioning of the SπRIT Time Projection Chamber," Journal of the Korean Physical Society **69**, 144–151 (2016).

[27]Y. Yano, "The RIKEN RI Beam Factory Project: A Report," Nucl. Inst. Meth. B **261**, 1009–1013 (2007).

[28]J. W. Lee, G. Jhang, G. Cerizza, J. Barney, J. Estee, T. Isobe, M. Kaneko, M. Kurata-Nishimura, W. G. Lynch, T. Murakami, C. Y. Tsang, M. B. Tsang, R. Wang, B. Hong, A. B. McIntosh, H. Sakurai, C. Santamaria, R. Shane, and Y. Zhang, "Charged particle track reconstruction with sπrit time projection chamber," Nuclear Instruments and Methods in Physics Research Section A: Accelerators, Spectrometers, Detectors and Associated Equipment **965**, 163840 (2020).

[29]C. Y.Tsang, J. Estee, R. Wang, J. Barney, G. Jhang, et al., "Space charge effects in the sπrit time projection chamber," Nuclear Instruments and Meth-

ods in Physics Research Section A: Accelerators, Spectrometers, Detectors and Associated Equipment **959**, 163477 (2020).

[30]"What are Cosmics?" `https://groups.nscl.msu.edu/hira/cosmic/WhatareCosmics.html`, accessed on April 11, 2020.

[31]W. Waltenberger, W. Mitaroff, and F. Moser, "Rave—a detector-independent vertex reconstruction toolkit," Nuclear Instruments and Meth-

ods in Physics Research Section A: Accelerators, Spectrometers, Detectors and Associated Equipment **581**, 549 (2007).